


 Cite this: *RSC Adv.*, 2024, 14, 14868

Received 22nd February 2024

Accepted 29th April 2024

DOI: 10.1039/d4ra01372g

[rsc.li/rsc-advances](https://rsc.li/rsc-advances)

# Synergistic effect between $\text{In}_2\text{O}_3$ and $\text{ZrO}_2$ in the reverse water gas shift reaction†

 Jiayu Dong,<sup>a</sup> Hong Wang,<sup>d</sup> Guofeng Zhao,<sup>id</sup>\*<sup>c</sup> Dong Jiang<sup>\*b</sup> and Haitao Xu<sup>id</sup>\*<sup>a</sup>

Efficient activation of  $\text{CO}_2$  at low temperature was achieved through the interface effect between  $\text{In}_2\text{O}_3$  and  $\text{ZrO}_2$  by their geometric and electronic effects. The results show that  $75\text{In}_2\text{O}_3\text{-}25\text{ZrO}_2$  ( $\text{In}_2\text{O}_3$  :  $\text{ZrO}_2$  molar ratio of 3 : 1), as a catalyst for the reverse water gas shift reaction, can achieve 28%  $\text{CO}_2$  conversion with 96% CO selectivity at 400 °C, 0.1 MPa, a  $\text{H}_2$  :  $\text{CO}_2$  molar ratio of 3 : 1 and a gas hourly space velocity of 10 000  $\text{mL g}^{-1} \text{h}^{-1}$ . *In situ* FTIR experiments provide a basis for clarifying the pivotal role of formate (facilitated at  $\text{In}_2\text{O}_3\text{-ZrO}_2$  interface) in this reaction.

## 1. Introduction

Throughout the course of industrial development, humans have heavily relied on fossil fuels to meet the substantial demand for energy, resulting in a continuous increase in greenhouse gas emissions and exacerbation of climate change.<sup>1</sup> Utilizing carbon dioxide, an abundant and economical carbon resource, to produce high-value-added chemicals or liquid fuels is of significant importance for energy conservation, emissions reduction, and the sustainable utilization of carbon resources.<sup>2</sup> In recent years, carbon capture and utilization (CCU) technology has attracted much attention and is considered as one of the useable ways to reduce  $\text{CO}_2$  emissions.<sup>3–7</sup> The thermal catalytic reduction of  $\text{CO}_2$  refers to the process of converting  $\text{CO}_2$  into hydrocarbons or carbon monoxide (CO) with green hydrogen, typically carried out with the aid of catalysts at elevated temperature.<sup>8</sup> The rapid development of renewable energy lowers the cost of green hydrogen production,<sup>9</sup> prompting the urgent need for catalysts with high activity, selectivity, and stability.

The reverse water gas shift (RWGS) reaction hydrogenates  $\text{CO}_2$  into CO, which can be further used to synthesize methanol, breaking through the thermodynamic equilibrium limit of direct methanol production from  $\text{CO}_2$ ,<sup>10,11</sup> and can also be

combined with Fischer–Tropsch synthesis (FTS) process to prepare useful chemicals such as olefins.<sup>12–15</sup> Whether producing methanol through the CAMERE method (carbon dioxide hydrogenation to form methanol *via* a RWGS reaction) or preparing low-carbon olefins *via* the  $\text{CO}_2$ -FTS method, the RWGS reaction with high CO yield is a crucial step. Therefore, the RWGS reaction is considered as the most promising and prospective pathway in re-utilizing  $\text{CO}_2$ .

Catalysts used in the RWGS reaction can be classified into noble metal catalysts, such as Rh,<sup>16</sup> Ru,<sup>17</sup> and Pt,<sup>18</sup> and non-noble metal catalysts, such as Co,<sup>19</sup> Fe,<sup>20,21</sup> and Mo.<sup>22,23</sup> The noble metal catalysts exhibit outstanding performance due to their effective hydrogen dissociation capabilities, but their high costs and instability (nanoparticle agglomeration) limit their industrial application; the non-noble metal catalysts need high temperature to deliver the same performance as noble metal ones.<sup>24</sup> Therefore, there is of significant importance in developing low-temperature, high-performance catalysts to address these limitations. In recent years, indium oxide ( $\text{In}_2\text{O}_3$ ) has been found as a proficient catalyst for  $\text{CO}_2$  hydrogenation, with its pronounced catalytic activity attributed to the abundant oxygen vacancy ( $\text{O}_v$ ) on its surface.<sup>25–28</sup> Furthermore,  $\text{In}_2\text{O}_3$  can be easily supported and/or modified by promoters to form more  $\text{O}_v$  sites, thereby activating more  $\text{CO}_2$  molecules, and stabilizing surface intermediates near  $\text{O}_v$ .<sup>29–33</sup>

Moreover,  $\text{ZrO}_2$  is also used as catalyst support in RWGS reaction, but its role plays in the reaction is still unclear.<sup>34</sup> Unfortunately, there are relatively few reports related to the synergistic interfacial effect between  $\text{In}_2\text{O}_3$  and  $\text{ZrO}_2$ , hampering the rational design of mixed oxides for the RWGS reaction. For the optimal  $75\text{In}_2\text{O}_3\text{-}25\text{ZrO}_2$  ( $\text{In}_2\text{O}_3$  :  $\text{ZrO}_2$  molar ratio of 3 : 1) with abundant  $\text{In}_2\text{O}_3\text{-ZrO}_2$  interface, 28%  $\text{CO}_2$  conversion and 96% CO selectivity can be achieved at 400 °C, 0.1 MPa,  $\text{H}_2$  :  $\text{CO}_2$  molar ratio of 3 : 1 and GHSV (gas hourly space velocity) of 10 000  $\text{mL g}^{-1} \text{h}^{-1}$ . Control experiments and characterization results testify that the as-formed oxygen

<sup>a</sup>School of Chemical Engineering, East China University of Science and Technology, Shanghai 200237, China. E-mail: xuhaitao@ecust.edu.cn

<sup>b</sup>School of Chemistry and Molecular Engineering, East China University of Science and Technology, Shanghai 200237, China. E-mail: jiangdong@ecust.edu.cn

<sup>c</sup>Key Laboratory of Functional Molecular Solids, Ministry of Education, College of Chemistry and Materials Science, Anhui Normal University, Wuhu 241002, China. E-mail: gfzhao@chem.enu.edu.cn

<sup>d</sup>Institute of Optical Functional Materials for Biomedical Imaging, School of Chemistry and Pharmaceutical Engineering, Shandong First Medical University, Shandong Academy of Medical Sciences, Taian 271016, China

 † Electronic supplementary information (ESI) available. See DOI: <https://doi.org/10.1039/d4ra01372g>


vacancies ( $O_{vs}$ ) caused by the reduction of  $In_2O_3$  to  $In_2O_{3-x}$  significantly enhance catalytic activity for  $75In_2O_3-25ZrO_2$ . In addition, *in situ* Fourier transform infrared spectroscopy (FTIR) shows that  $HCOO^*$  (formate) plays an important role in this reaction. For  $75In_2O_3-25ZrO_2$  with abundant  $In_2O_3-ZrO_2$  interface,  $HCOO^*$  is easily hydrogenated into CO. However, for  $In_2O_3$ , the content of  $HCOO^*$  is relatively lower, thus contributing to its lower catalytic activity. For  $ZrO_2$ , the  $CO_3^{2-}$  is relatively stable, correlating well with its low catalytic activity. This work elucidates the synergistic effect between mixed  $In_2O_3$  and  $ZrO_2$ , paving a way to design industrial catalyst with abundant  $In_2O_3-ZrO_2$  interface to offer excellent catalytic performance for RWGS reaction.

## 2. Experimental

### 2.1. Catalyst preparation

The mixed In–Zr oxides were synthesized by a co-precipitation method. For instance, for the  $75In_2O_3-25ZrO_2$  ( $In_2O_3:ZrO_2$  molar ratio of 3:1), 1.5612 g  $In(NO_3)_3 \cdot xH_2O$  and 0.3713 g  $Zr(NO_3)_4 \cdot 5H_2O$  were dissolved in 20 mL deionized water, followed by the addition of the mixed solution of  $NH_4OH$  (10 mL, 25 wt% in  $H_2O$ , Alfa Aesar) and ethanol (30 mL, Titan) until the pH reaching 9.2. The resulting slurry was heated to 80 °C with vigorous stirring and aged for 30 min. Then the solid was separated by high-pressure filtration, washed with 500 mL deionized water, dried at 60 °C for 12 h, and calcined at 500 °C (heating rate of ca. 2 °C  $min^{-1}$ ) for 3 h. Other catalysts such as  $In_2O_3$ ,  $ZrO_2$ , and  $aIn_2O_3-bZrO_2$  ( $a$  and  $b$  represent  $In_2O_3$  and  $ZrO_2$  molar ratio ( $a = 25\%$ ,  $50\%$ , and  $75\%$ ,  $b = 1 - a$ )) were prepared using the same method by simply tuning the molar ratio of  $In(NO_3)_3 \cdot xH_2O$  and  $Zr(NO_3)_4 \cdot 5H_2O$ .

### 2.2. Catalyst characterization

The  $N_2$  sorption was conducted using the ASAP 2020 instrument (Mack, USA). The specific surface area ( $S_{BET}$ ) was determined by Brunauer–Emmett–Teller (BET) model and the pore size was calculated by Barret–Joyner–Halenda (BJH) model. The In and Zr loadings were detected by an inductively coupled plasma-atomic emission spectrometry (ICP-AES) at 167–785 nm/725 instrument (Agilent Corporation, USA). The power X-ray diffraction (XRD) patterns of catalysts were obtained on a Rigaku D/Max 2550 VB/PC instrument (Rigaku, Japan) using a scanning rate of 10°  $min^{-1}$ . The fine structures were observed by a transmission electron microscopy (TEM) at an accelerating voltage of 200 kV on JEM-2100 (JEOL, Japan). The energy dispersive X-ray spectroscopy (EDX) was measured by the JEM-2100 (JEOL, Japan) with an amplification of 8000–300 000. X-ray photoelectron spectroscopy (XPS) was measured at ESCALAB 250Xi photoelectron spectrometer (Thermo Fisher Scientific, USA) equipped with an Al-K $\alpha$  X-ray source. All the binding energies were calibrated on the basis of the internal standard of the binding energy of C 1s (284.8 eV). Electron paramagnetic resonance (EPR) spectroscopy was performed using the CIQTEK EPR200-Plus. Spectra were collected accumulating 1 scan for field sweeps of 3250–3850 G at 298 K with a magnetic field

modulation frequency of 100 kHz. The spectrum of an empty tube was subtracted to correct for the background signal.

The experiments of  $H_2$ -temperature programmed reduction ( $H_2$ -TPR) and  $CO_2$ -temperature programmed desorption ( $CO_2$ -TPD) were carried out on a ChemBET Pulsar automatic adsorption apparatus (Quantachrome Company, USA) equipped with a thermal conductivity detector (TCD), and the efflux were monitored by an on-line mass spectrometer (MS, SHP8400PMS-L, Shanghai Sunny Hengping Scientific Instrument Co. Ltd, China). For  $H_2$ -TPR, each catalyst (0.1 g) was pretreated in Ar flow (30 mL  $min^{-1}$ ) at 300 °C for 0.5 h and cooled down to room temperature. Then, the gas was switched to  $H_2/Ar$  flow (10 vol%  $H_2$ , 50 mL  $min^{-1}$ ) and the catalyst was reduced from room temperature to 800 °C at a heating rate of 10 °C  $min^{-1}$ . For  $CO_2$ -TPD, each catalyst (0.1 g) was pretreated in Ar flow (30 mL  $min^{-1}$ ) at 400 °C for 1 h, and then reacted in mixture gas (the molar ratio of  $H_2:CO_2$  is 3:1, 50 mL  $min^{-1}$ ) at 400 °C for 2 h. Then, the catalyst was cooled to 50 °C in the same flow followed by  $CO_2$  (50 mL  $min^{-1}$ ) adsorption at 50 °C for 2 h. After that, the catalyst was flushed in He flow (50 mL  $min^{-1}$ ) for 0.5 h, followed by heated from 50 to 800 °C at a rate of 10 °C  $min^{-1}$ , and signals of  $CO_2$  were monitored by MS on line.

The *in situ* Fourier transform infrared (FT-IR) was conducted on a IRPrestige-21 equipment (Shimadzu, Japan). A resolution of 8  $cm^{-1}$  and scanning times of 50. 50 mg catalyst and 100 mg KBr were pressed into a wafer and placed in the *in situ* chamber. All the samples were pretreated at 400 °C in  $H_2$  flow (37.5 mL  $min^{-1}$ ) for 10 min and cooled to the room temperature to obtain the background spectrum. When the adsorption of  $CO_2$ , the flow was switched to  $CO_2$  (12.5 mL  $min^{-1}$ , 99.99%) at room temperature for 10 min, after that,  $CO_2$  was switched off and the catalyst was maintained at 50 °C for 2 h. Subsequently, catalyst was purged with a He flow (30 mL  $min^{-1}$ ) for 5 minutes and then raised from 50 to 400 °C, with the spectra were collected. After raising to 400 °C, the flow was switched to  $H_2$  for 10 s,  $H_2$  was switched off and the spectra was collected at 0.5 MPa. When the co-adsorption of  $CO_2$  and  $H_2$ , the flow was switched to the mixed gas (the molar ratio of  $H_2:CO_2$  is 3:1, 50 mL  $min^{-1}$ ). The temperature was raised from 100 to 400 °C and the spectra were collected.

### 2.3. Catalytic evaluation

In this work, a continuous fixed-bed reactor was used to evaluate the performance of catalysts. Typically, 0.3 g catalyst was loaded into a reactor with an inner diameter of 7 mm and the length of 700 mm.  $H_2$  (36 mL  $min^{-1}$ ),  $CO_2$  (12 mL  $min^{-1}$ ), and Ar (2 mL  $min^{-1}$ ) was controlled by mass flow controllers, forming a  $H_2/CO_2/Ar$  (molar ratio of 72/24/4) mixture and passing through the catalyst bed. The Ar was used as the internal standard gas. Then, the temperature was successively raised from room temperature to 400 °C and maintained for 2 h. The effluent was analyzed by online gas chromatography (GC7900), equipped with a thermal conductivity detector (TCD) and TDX-1 column. The  $CO_2$  conversion ( $X_{CO_2}$ ), CO selectivity ( $S_{CO}$ ), CO yield ( $Y_{CO}$ ) and  $CH_4$  selectivity ( $S_{CH_4}$ ) were calculated as follows:



$$X_{\text{CO}_2} = \frac{\text{CO}_2^{\text{in}} - \text{CO}_2^{\text{out}}}{\text{CO}_2^{\text{in}}} \times 100\% \quad (1)$$

$$S_{\text{CO}} = \frac{\text{CO}^{\text{out}}}{\text{CO}_2^{\text{in}} - \text{CO}_2^{\text{out}}} \times 100\% \quad (2)$$

$$Y_{\text{CO}} = X_{\text{CO}_2} \times S_{\text{CO}} \quad (3)$$

$$S_{\text{CH}_4} = \frac{\text{CH}_4^{\text{out}}}{\text{CO}_2^{\text{in}} - \text{CO}_2^{\text{out}}} \times 100\% \quad (4)$$

$\text{CO}_2^{\text{in}}$  and  $\text{CO}_2^{\text{out}}$  represent the concentration of  $\text{CO}_2$  at the inlet and outlet, respectively;  $\text{CO}^{\text{out}}$  represents the concentration of CO at the outlet;  $\text{CH}_4^{\text{out}}$  represent the concentration of CH<sub>4</sub> at the outlet.

### 3. Results and discussion

#### 3.1. Structures and chemical states of fresh catalysts

Five  $\text{In}_2\text{O}_3$ - $\text{ZrO}_2$  catalysts were prepared by the co-precipitation method, varying the molar content of  $\text{In}_2\text{O}_3$  of 0, 25%, 50%, 75% and 100%. The inductively coupled plasma-atomic emission spectrometry (ICP-OES) measurements confirmed that In and Zr contents were almost identical to the theoretical value. Adding  $\text{ZrO}_2$  to  $\text{In}_2\text{O}_3$  will slightly increase the specific surface area (Table S1<sup>†</sup>), but the specific surface area of  $75\text{In}_2\text{O}_3$ - $25\text{ZrO}_2$  is close to that of  $\text{In}_2\text{O}_3$ , albeit the catalyst area is not the key factor determining catalytic activity.<sup>35</sup> Moreover, the type IV hysteresis loop testifies the mesoporous structure of this series of catalysts (Fig. S1<sup>†</sup>). TEM images of this series of catalysts show the similar morphologies, with the diameter of 8–15 nm (Fig. S2<sup>†</sup>).

For  $75\text{In}_2\text{O}_3$ - $25\text{ZrO}_2$ , the average particle size is 10.0 ± 1.4 nm, and the HRTEM images illustrate the lattice distances of 0.292, 0.275, and 0.297 nm, corresponding to the  $\text{In}_2\text{O}_3$ (222),  $\text{In}_2\text{O}_3$ (321), and  $t$ - $\text{ZrO}_2$ (101) planes, respectively (Fig. S3a and b<sup>†</sup>). The STEM-EDX mapping images show that In and Zr elements are randomly distributed on the catalyst surface (Fig. S3c and d<sup>†</sup>), forming abundant  $\text{In}_2\text{O}_3$ - $\text{ZrO}_2$  interface and tentatively contributing to excellent catalytic performance.

X-ray diffraction (XRD) was used to figure out the effect of Zr modification on bulk structure. The XRD patterns in Fig. S4a,<sup>†</sup> display that the pure  $\text{ZrO}_2$  (*i.e.*,  $0\text{In}_2\text{O}_3$ - $100\text{ZrO}_2$ ) prefers to crystallize to its thermodynamically stable monoclinic structure; the presence of In steers the growth of  $\text{ZrO}_2$  toward metastable tetragonal phase,<sup>28</sup> suggesting that partial In is incorporated into the  $\text{ZrO}_2$  lattice in the form of In–O–Zr bond, as evidenced by the HRTEM image of  $75\text{In}_2\text{O}_3$ - $25\text{ZrO}_2$  sample.<sup>36</sup> The transition from In–O–In bond to In–O–Zr bond should greatly improve the  $\text{CO}_2$  conversion and CO selectivity of  $\text{In}_2\text{O}_3$ - $\text{ZrO}_2$  catalysts (see the results in Section 3.2). Owing to the fact that the lattice parameters of cubic  $\text{In}_2\text{O}_3$  (JCPDS card 06-0416) and  $t$ - $\text{ZrO}_2$  (JCPDS card 37-1413) are akin, their XRD patterns are virtually identical. However, as shown in Fig. S4b,<sup>†</sup> the diffraction peak moves from  $30.167^\circ$  ( $t$ - $\text{ZrO}_2$ (111)) to  $30.580^\circ$  ( $c$ - $\text{In}_2\text{O}_3$ (222)) with the increase of  $\text{In}_2\text{O}_3$  content, and such tiny peak shift confirms the generation of  $\text{In}_2\text{O}_3$ - $\text{ZrO}_2$  solid solution.

The surface chemical states of  $\text{In}_2\text{O}_3$ - $\text{ZrO}_2$  catalysts were characterized by XPS (Fig. 1) and EPR (Fig. S6<sup>†</sup>). The symmetric binding energy peaks at ~452 and ~444.3 eV testify that In species exists in the form of  $\text{In}^{3+}$ .<sup>37</sup> With the increase of  $\text{In}_2\text{O}_3$  content, the binding energy of  $\text{In}^{3+}$  decreases slightly, indicating the electron transfer from Zr to In.<sup>36</sup> The symmetric binding energy peaks at ~184.5 and ~182.0 eV testify that Zr species exists in the form of  $\text{Zr}^{4+}$ .<sup>38</sup> For  $50\text{In}_2\text{O}_3$ - $50\text{ZrO}_2$  and  $75\text{In}_2\text{O}_3$ - $25\text{ZrO}_2$ , the binding energies of Zr are higher than that of  $25\text{In}_2\text{O}_3$ - $75\text{ZrO}_2$ , also coinciding with the electron transfer. For the O 1s XPS spectra, the major peak at 529.5–531.0 eV corresponds to lattice oxygen, the peak at 531.0–532.0 eV to  $\text{O}_v$ , and the one at 532.5–533.0 eV to surface OH.<sup>39</sup> Obviously, with the increase of  $\text{In}_2\text{O}_3$  content, the  $\text{O}_v$  content increases progressively. Fig. S5<sup>†</sup> shows that there is a positive correlation between the CO STY (space-time yield) and the oxygen vacancy concentration, which means that the  $\text{O}_v$  may play an important role in the RWGS reaction. Furthermore, the EPR results in Fig. S6<sup>†</sup> reveals a signal of  $g = 1.890$  for fresh  $\text{In}_2\text{O}_3$ , which implies that the surface vacancies exist on  $\text{In}_2\text{O}_3$ .<sup>40</sup> Pure  $\text{ZrO}_2$  sample exhibits an isotropic EPR signal at  $g = 1.973$ , which is assigned to the bulk  $\text{Zr}^{3+}$  ions located at axially symmetric sites. The  $75\text{In}_2\text{O}_3$ - $25\text{ZrO}_2$  demonstrates a prominent signal that can be attributed to unpaired electrons trapped in symmetric site at  $g$

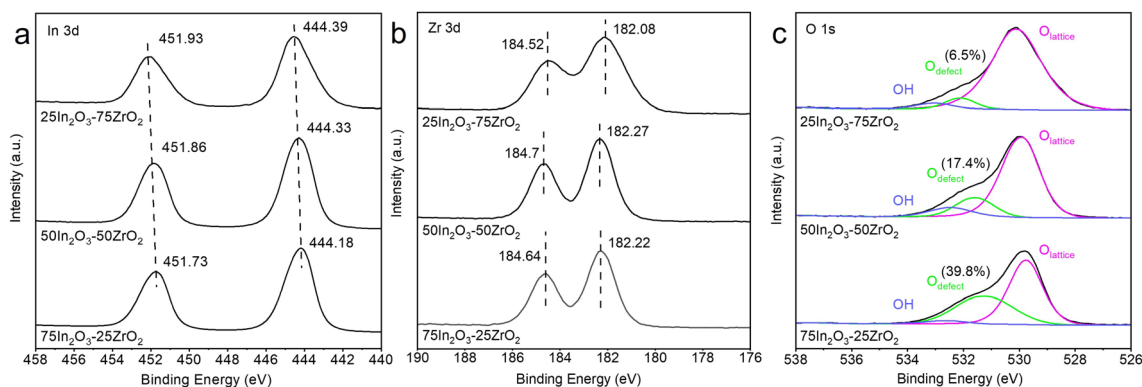


Fig. 1 XPS spectra of (a) In 3d, (b) Zr 3d, and (c) O 1s for the  $25\text{In}_2\text{O}_3$ - $75\text{ZrO}_2$ ,  $50\text{In}_2\text{O}_3$ - $50\text{ZrO}_2$  and  $75\text{In}_2\text{O}_3$ - $25\text{ZrO}_2$  catalyst.



= 2.004, which is always typically assigned to oxygen vacancies.<sup>41</sup> This means the synergistic effect between In<sub>2</sub>O<sub>3</sub> and ZrO<sub>2</sub> in 75In<sub>2</sub>O<sub>3</sub>-25ZrO<sub>2</sub> solid solution is beneficial to produce new oxygen vacancies at  $g = 2.004$ , which is in line with the XPS result.

H<sub>2</sub> temperature-programmed reduction (H<sub>2</sub>-TPR) tests were conducted to determine the reactivity of the In<sub>2</sub>O<sub>3</sub>-ZrO<sub>2</sub> catalyst toward H<sub>2</sub> activation in the temperature range of 50–800 °C, as shown in Fig. S7a.† The H<sub>2</sub>-TPR profiles revealed that reduction temperature of bulk In<sub>2</sub>O<sub>3</sub> in In<sub>2</sub>O<sub>3</sub> and 75In<sub>2</sub>O<sub>3</sub>-25ZrO<sub>2</sub> are 662 °C and 697 °C respectively, while the reduction temperature of surface In<sub>2</sub>O<sub>3</sub> are 189 °C and 225 °C respectively. However, the H<sub>2</sub>-TPR of ZrO<sub>2</sub> demonstrates no significant H<sub>2</sub> consumption, which means the neglectable reducibility of ZrO<sub>2</sub>. Interestingly, for 75In<sub>2</sub>O<sub>3</sub>-25ZrO<sub>2</sub>, the reduction signals of surface and the bulk In<sub>2</sub>O<sub>3</sub> are located at a higher temperature than that of pure In<sub>2</sub>O<sub>3</sub> catalyst, hinting a stronger interaction between In<sub>2</sub>O<sub>3</sub> and ZrO<sub>2</sub>.<sup>29</sup> This also shows the increasing O<sub>v</sub> content over 75In<sub>2</sub>O<sub>3</sub>-25ZrO<sub>2</sub> catalyst, which is in accordance with the XPS result and the prominent catalytic activity.<sup>42</sup>

CO<sub>2</sub> temperature programmed desorption (CO<sub>2</sub>-TPD) was conducted to further investigate the CO<sub>2</sub> adsorption behaviour on the In<sub>2</sub>O<sub>3</sub>-ZrO<sub>2</sub> catalyst, as shown in Fig. S7b.† The profiles exhibit several significant CO<sub>2</sub> evolution signals from the ZrO<sub>2</sub> and 75In<sub>2</sub>O<sub>3</sub>-25ZrO<sub>2</sub> catalyst in the temperature range of 134–220, 273–315 and 396–477 °C. While the signal of CO<sub>2</sub> adsorbed on pure In<sub>2</sub>O<sub>3</sub> are not detectable. The signal peak around 153 °C belongs to the physisorption of CO<sub>2</sub>. Other signal peaks belong to the chemically absorbed CO<sub>2</sub> on the H<sub>2</sub>-induced oxygen vacancy sites (O<sub>v</sub>).<sup>42</sup> Additionally, CO<sub>2</sub>-TPD has been widely used to measure the surface basicity of catalysts, and high desorption temperature promised a strong basic site.<sup>43</sup> Compared with ZrO<sub>2</sub> catalyst, the CO<sub>2</sub> desorption peak of 75In<sub>2</sub>O<sub>3</sub>-25ZrO<sub>2</sub> catalyst shift to the higher temperatures of 315 °C and 75In<sub>2</sub>O<sub>3</sub>-25ZrO<sub>2</sub> catalyst have strong site at around 450 °C. Specifically, the addition of In enhances the strength of CO<sub>2</sub> adsorption on these sites, owing to the increase in basic intensity.<sup>42</sup> The characterization results of H<sub>2</sub>-TPR and CO<sub>2</sub>-TPD consistently confirm that In<sub>2</sub>O<sub>3</sub>-ZrO<sub>2</sub> interface benefits the formation of oxygen vacancies, thus enhancing the ability of 75In<sub>2</sub>O<sub>3</sub>-25ZrO<sub>2</sub> catalyst to CO<sub>2</sub> adsorption and H<sub>2</sub> activation.

### 3.2. Catalytic performance

CO<sub>2</sub> hydrogenation mainly involves the following three reactions (5)–(7) to produce three products of CO, CH<sub>4</sub> and CH<sub>3</sub>OH, respectively.

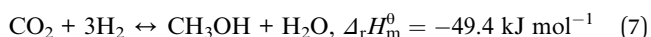
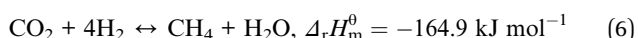
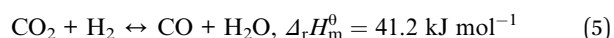


Fig. 2a shows the CO<sub>2</sub> conversion, CO selectivity, and CO yield over the five catalysts. The catalytic performance of pure ZrO<sub>2</sub> (*i.e.*, 0In<sub>2</sub>O<sub>3</sub>-100ZrO<sub>2</sub>) is extremely poor, with CO<sub>2</sub> conversion of only 4% and CO selectivity of only 53%, while the

pure In<sub>2</sub>O<sub>3</sub> (*i.e.*, 100In<sub>2</sub>O<sub>3</sub>-0ZrO<sub>2</sub>) gives higher CO<sub>2</sub> conversion of 23.5% and CO selectivity of 95.8%. Interestingly, the In<sub>2</sub>O<sub>3</sub>-ZrO<sub>2</sub> catalysts (*i.e.*, 25In<sub>2</sub>O<sub>3</sub>-75ZrO<sub>2</sub>, 50In<sub>2</sub>O<sub>3</sub>-50ZrO<sub>2</sub>, and 75In<sub>2</sub>O<sub>3</sub>-25ZrO<sub>2</sub>) all offers CO selectivity above 92%, with volcano evolution of CO<sub>2</sub> conversion. Most notably, the 75In<sub>2</sub>O<sub>3</sub>-25ZrO<sub>2</sub> offers the highest CO selectivity of 96% and highest CO<sub>2</sub> conversion of 28%. Due to a pronounced synergistic effect between ZrO<sub>2</sub> and In<sub>2</sub>O<sub>3</sub>, the In-Zr interface within the bimetallic oxides augments the density of O<sub>v</sub> on the In<sub>2</sub>O<sub>3</sub> surface, thereby significantly enhancing the adsorption and hydrogenation capacities towards CO<sub>2</sub>. In addition, no methane can be detected, and a small amount of methanol was the only by-product.

The influence of reaction temperature, pressure, and gas hourly space velocity (GHSV) on catalytic performance is exhibited in Fig. 2b, c and S8.† At 0.1 MPa, and GHSV of 10 000 mL g<sup>-1</sup> h<sup>-1</sup>, with the temperature rising from 300 to 500 °C, CO<sub>2</sub> conversion increases from 4% to 44%, and the highest CO selectivity is 96% at 400 °C. At 400 °C, and GHSV of 10 000 mL g<sup>-1</sup> h<sup>-1</sup>, with the pressure increasing from 0.1 to 4 MPa, CO<sub>2</sub> conversion slightly increases from 28% to 29%, but CO selectivity decreases from 96% to 85% (with the formation of new by-product CH<sub>4</sub>), because high reaction pressure is beneficial to CO<sub>2</sub> methanation reaction.<sup>44</sup> Moreover, at 0.1 MPa, and 400 °C, CO<sub>2</sub> conversion decreases from 35% to 27.7% with increasing GHSV from 6000 to 14 000 mL g<sup>-1</sup> h<sup>-1</sup>, while the maximum CO selectivity is 94% at the GHSV of 10 000 mL g<sup>-1</sup> h<sup>-1</sup>. Hence, the optimized reaction condition is as follows: 0.1 MPa, 400 °C and GHSV of 10 000 mL g<sup>-1</sup> h<sup>-1</sup>. For the best catalyst 75In<sub>2</sub>O<sub>3</sub>-25ZrO<sub>2</sub>, under the best reaction conditions, the CO<sub>2</sub> conversion and CO selectivity are 28% and 96% in the 200 h-test. However, for In<sub>2</sub>O<sub>3</sub>, the conversion decreases from 26% to 21%. Compared with pure In<sub>2</sub>O<sub>3</sub>, the stability of mixed oxides is obviously enhanced. Hence, the In<sub>2</sub>O<sub>3</sub>-ZrO<sub>2</sub> interface is of great importance in improving and maintaining catalytic activity (Fig. 2d). We compared the catalyst 75In<sub>2</sub>O<sub>3</sub>-25ZrO<sub>2</sub> with other catalysts including non-noble metal and noble metal catalysts in the RWGS reaction in Table S3.† CO<sub>2</sub> conversion, CO selectivity and STY of 75In<sub>2</sub>O<sub>3</sub>-25ZrO<sub>2</sub> are very promising. Notably, the STY of 75In<sub>2</sub>O<sub>3</sub>-25ZrO<sub>2</sub> is higher than other catalysts (apart from Ag/Al<sub>2</sub>O<sub>3</sub>). Furthermore, compared with noble metal catalysts, In-based catalysts have lower cost and more prospects in industry applications.

### 3.3. Surface intermediates and reaction mechanism

*In situ* FTIR was used to investigate the evolution of key surface intermediates for RWGS reaction, and the wavenumbers of the intermediates are summarized in Table S4.†<sup>33,34,36,37,39,45-55</sup> Firstly, the three catalysts (75In<sub>2</sub>O<sub>3</sub>-25ZrO<sub>2</sub>, In<sub>2</sub>O<sub>3</sub>, and ZrO<sub>2</sub>) were placed into the chamber and reduced with hydrogen at 400 °C. Subsequently, CO<sub>2</sub> was introduced into the chamber for adsorption. Finally, the gaseous CO<sub>2</sub> was purged by He flow and the spectra were collected from 50 to 400 °C (Fig. 3). For 75In<sub>2</sub>O<sub>3</sub>-25ZrO<sub>2</sub> (Fig. 3a), the following characteristic bands can be observed: bi-HCOO\* (bidentate formate, at 1350, 1589, 2873 and 2967 cm<sup>-1</sup>);<sup>33,36,39,46,48,50,52-55</sup> b-\*OCH<sub>3</sub> (bridged methoxy, at





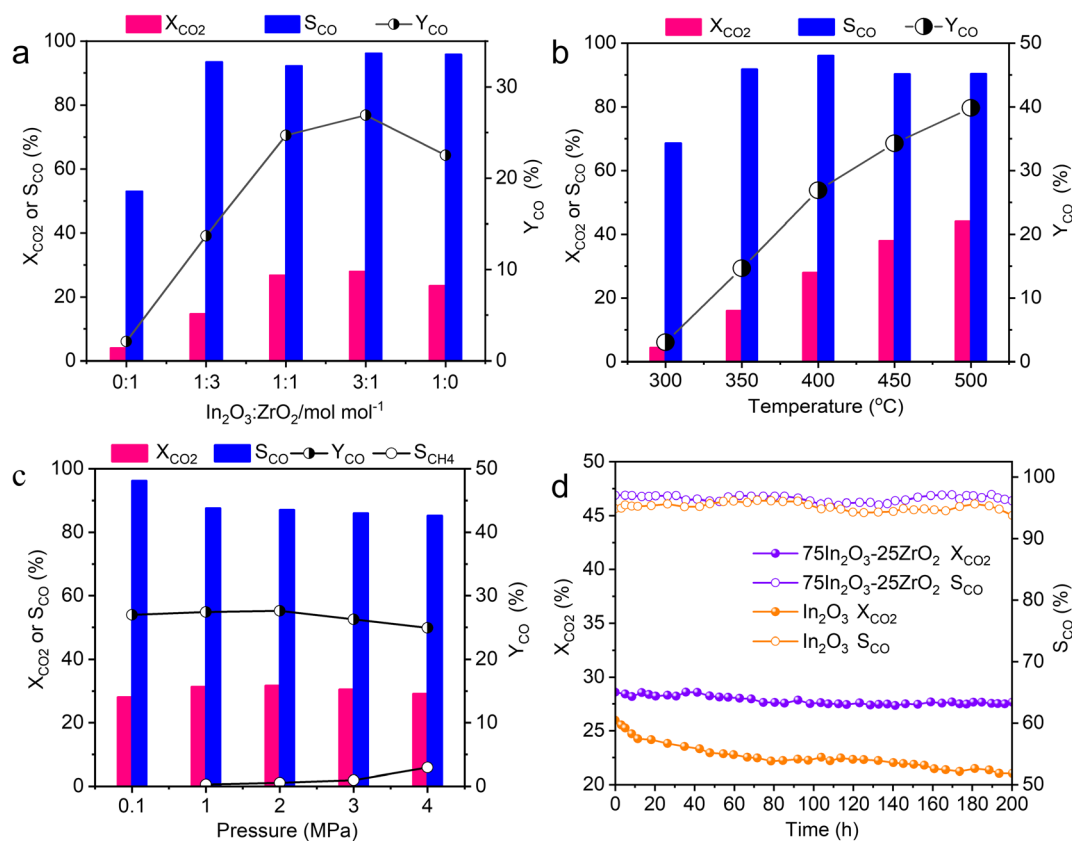


Fig. 2 (a) The catalytic performance of the  $In_2O_3-ZrO_2$  catalysts with different  $In_2O_3$  ratio (reaction conditions:  $400\ ^{\circ}C$ ,  $0.1\ MPa$ ,  $H_2 : CO_2 : Ar$  ratio =  $72 : 24 : 4$ ,  $10\ 000\ mL\ g^{-1}\ h^{-1}$ ); (b) influence of reaction temperature on the catalytic performance of  $75In_2O_3-25ZrO_2$  (reaction conditions:  $0.1\ MPa$ ,  $H_2 : CO_2 : Ar$  ratio =  $72 : 24 : 4$ ,  $10\ 000\ mL\ g^{-1}\ h^{-1}$ ); (c) influence of pressure on the catalytic performance of  $75In_2O_3-25ZrO_2$  (reaction conditions:  $400\ ^{\circ}C$ ,  $H_2 : CO_2 : Ar$  ratio =  $72 : 24 : 4$ ,  $10\ 000\ mL\ g^{-1}\ h^{-1}$ ); (d) the stability test of  $75In_2O_3-25ZrO_2$  and  $In_2O_3$  (reaction conditions:  $400\ ^{\circ}C$ ,  $0.1\ MPa$ ,  $H_2 : CO_2 : Ar$  ratio =  $72 : 24 : 4$ ,  $10\ 000\ mL\ g^{-1}\ h^{-1}$ ).

1128, 2822 and  $2930\ cm^{-1}$ ).<sup>33,39,50-53</sup> With the increase of temperature, the peak area of bi-HCOO\* increases significantly, testifying that  $CO_2$  could be transformed into bi-HCOO\* easily. For  $In_2O_3$  (Fig. 3b), similar characteristic bands are also found, but the content of bi-HCOO\* is relatively lower, corresponding well with its lower catalytic activity and tentatively showing that bi-HCOO\* may play an important role in this reaction. For  $ZrO_2$  (Fig. 3c), the following characteristic bands can be observed: bi- $HCO_3^-$  (bidentate bicarbonate, at  $1284$  and  $1636\ cm^{-1}$ ),<sup>34,49,54</sup> m- $CO_3^{2-}$  (monodentate carbonate, at  $1355\ cm^{-1}$ ),<sup>34,49</sup> bi- $CO_3^{2-}$  (bidentate carbonate, at  $1523\ cm^{-1}$ ),<sup>34,47</sup> p- $CO_3^{2-}$  (polydentate carbonate, at  $1463$  and  $1411\ cm^{-1}$ ),<sup>47,48,54</sup> b\*- $OCH_3$  (bridged

methoxy, at  $1126$ ,  $2830$  and  $2925\ cm^{-1}$ ).<sup>33,39,50-53</sup> With the increase of temperature, bi- $HCO_3^-$  decomposes rapidly, while bi- $CO_3^{2-}$  and m- $CO_3^{2-}$  decompose sluggishly. Because of with strong thermal resistance and a rather low separation between the two C-O stretching modes, polydentate carbonate species is relatively stable ( $\nu_{as}(CO_3) = 1463\ cm^{-1}$  and  $\nu_s(CO_3) = 1411\ cm^{-1}$ ).<sup>54</sup> In addition, the peak area of p- $CO_3^{2-}$  increases slightly, indicating that the above species may transform into p- $CO_3^{2-}$ .<sup>37</sup>

In order to testify the pivotal role of bi-HCOO\* playing in this reaction, the reaction of  $H_2$  and  $CO_2$  (molar ratio of  $H_2$  and  $CO_2$  is  $3 : 1$ ) over these three reduced catalysts were tracked by *in situ*

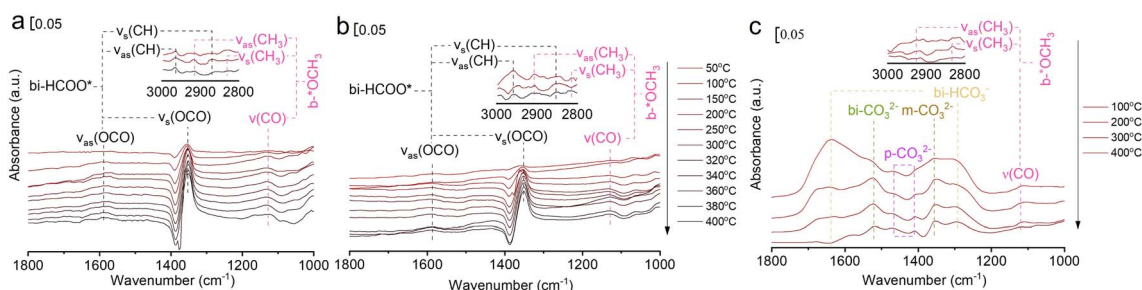


Fig. 3 *In situ* FTIR spectra of  $CO_2$  adsorption at different temperatures over (a)  $75In_2O_3-25ZrO_2$ , (b)  $In_2O_3$ , and (c)  $ZrO_2$ .



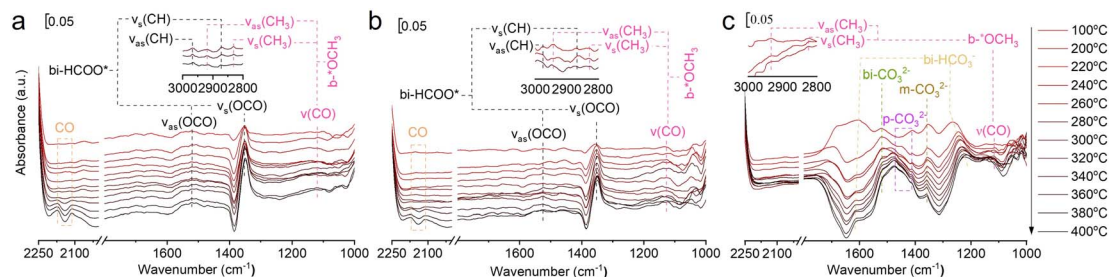


Fig. 4 *In situ* FTIR spectra of the reaction of CO<sub>2</sub> and H<sub>2</sub> over (a) 75In<sub>2</sub>O<sub>3</sub>-25ZrO<sub>2</sub>, (b) In<sub>2</sub>O<sub>3</sub>, and (c) ZrO<sub>2</sub>.

FTIR (Fig. 4). For 75In<sub>2</sub>O<sub>3</sub>-25ZrO<sub>2</sub>, the characteristic band of CO is observed at 320 °C ( $\nu(\text{CO}) = 2111.1$  and  $2170 \text{ cm}^{-1}$ ). However, for In<sub>2</sub>O<sub>3</sub>, CO starts to appear at 360 °C, corresponding well with its lower catalytic activity. For ZrO<sub>2</sub>, the characteristic bands of CO are not observed, showing that bi-HCO<sub>3</sub><sup>-</sup>, bi-CO<sub>3</sub><sup>2-</sup>, m-CO<sub>3</sub><sup>2-</sup>, and p-CO<sub>3</sub><sup>2-</sup> can't be hydrogenated easily.<sup>48</sup> Lastly, for all the three catalysts, b-OCH<sub>3</sub><sup>\*</sup> is also observed, but this species could only be hydrogenated to CH<sub>4</sub> at relative higher 0.5 MPa, thus excluding the role of OCH<sub>3</sub><sup>\*</sup> playing under the reaction conditions (Fig. S9†). But the CH<sub>4</sub> is not formed in the real fixed-bed reaction process, which is likely caused by the different conditions between *in situ* FTIR and real reaction process.

Combined with the above analyses, it can be suggested that CO<sub>2</sub> hydrogenation on the In<sub>2</sub>O<sub>3</sub>-ZrO<sub>2</sub> catalyst through HCOO\* intermediates (Scheme S1†). H<sub>2</sub> adsorbed on the exposed surface of In<sub>2</sub>O<sub>3</sub> crystal to form H<sub>2</sub><sup>\*</sup>, and then formed H<sub>in</sub><sup>\*</sup> and H<sub>O</sub><sup>\*</sup> at In site and O site, respectively. At the same time, CO<sub>2</sub> is adsorbed on a base on the surface of the composite oxide, activated by oxygen vacancy, and then combined with activated H<sub>in</sub><sup>\*</sup> to form formate intermediate (HCOO\*). HCOO\* interacts with the site of ZrO<sub>2</sub>, undergoes the cleavage of C-O and C-H bonds, and forms O-H bonds at the same time, producing CO\* and OH\*, and CO\* desorbs to produce CO.<sup>33,37</sup> In this case, ZrO<sub>2</sub> can not only modify In<sub>2</sub>O<sub>3</sub>, but also serve as an active site. In<sub>2</sub>O<sub>3</sub>-ZrO<sub>2</sub> constitutes a bimetallic In-Zr oxide catalyst system.

## 4. Conclusions

In this work, the optimal 75In<sub>2</sub>O<sub>3</sub>-25ZrO<sub>2</sub> and the contrastive In<sub>2</sub>O<sub>3</sub>, ZrO<sub>2</sub> were prepared by the coprecipitation method, and 75In<sub>2</sub>O<sub>3</sub>-25ZrO<sub>2</sub> exhibits excellent 28% conversion and 96% selectivity in the RWGS reaction under the best reaction conditions (400 °C, 0.1 MPa, H<sub>2</sub> : CO<sub>2</sub> molar ratio of 3 : 1 and gas hourly space velocity of  $10\,000 \text{ mL g}^{-1} \text{ h}^{-1}$ ). XRD and STEM-EDX show that the In<sub>2</sub>O<sub>3</sub>-ZrO<sub>2</sub> solid solution is formed, and XPS testifies that the electron transfer effect plays an important role in this reaction. *In situ* FTIR shows that: for 75In<sub>2</sub>O<sub>3</sub>-25ZrO<sub>2</sub> with abundant In<sub>2</sub>O<sub>3</sub>-ZrO<sub>2</sub> interface, HCOO\* is easily hydrogenated into CO; however, for In<sub>2</sub>O<sub>3</sub>, the content of HCOO\* is relatively lower, thus contributing to its lower catalytic activity; for ZrO<sub>2</sub>, the CO<sub>3</sub><sup>2-</sup> is relatively stable, correlating well with its low catalytic activity. This work definitely testifies the pivotal role of HCOO\* in the RWGS reaction, but also paves a way to design bimetal oxide catalyst with excellent catalytic performance for RWGS reaction.

## Conflicts of interest

The authors declare that there is no conflict of interest.

## References

- 1 S. J. Davis, K. Caldeira and H. D. Matthews, *Science*, 2010, **329**, 1330–1333.
- 2 Z. Zhang, S.-Y. Pan, H. Li, J. Cai, A. G. Olabi, E. J. Anthony and V. Manovic, *Renewable Sustainable Energy Rev.*, 2020, **125**, 109799.
- 3 A. Al-Mamoori, A. Krishnamurthy, A. A. Rownaghi and F. Rezaei, *Energy Technol.*, 2017, **5**, 834–849.
- 4 A. Kaetelhoe, R. Meys, S. Deutz, S. Suh and A. Bardow, *Proc. Natl. Acad. Sci. U. S. A.*, 2019, **116**, 11187–11194.
- 5 I. Mohsin, T. A. Al-Attas, K. Z. Sumon, J. Bergerson, S. McCoy and M. G. Kibria, *Cell Rep. Phys. Sci.*, 2020, **1**, 100104.
- 6 L. J. Mueller, A. Kaetelhoe, M. Bachmann, A. Zimmermann, A. Sternberg and A. Bardow, *Front. Energy Res.*, 2020, **8**, 15.
- 7 E. Kawai, A. Ozawa and B. D. Leibowicz, *Appl. Energy*, 2022, **328**, 120183.
- 8 T. Len and R. Luque, *Green Chem.*, 2023, **25**, 490–521.
- 9 Y. H. Zheng, M. Ma and H. Y. Shao, *Carbon Neutrality*, 2023, **2**, 23.
- 10 O. S. Joo, K. D. Jung, I. Moon, A. Y. Rozovskii, G. I. Lin, S. H. Han and S. J. Uhm, *Ind. Eng. Chem. Res.*, 1999, **38**, 1808–1812.
- 11 S. W. Park, O. S. Joo, K. D. Jung, H. Kim and S. H. Han, *Appl. Catal., A*, 2001, **211**, 81–90.
- 12 R. Liu, D. Leshchev, E. Stavitski, M. Juneau, J. N. Agwara and M. D. Porosoff, *Appl. Catal., B*, 2021, **284**, 119787.
- 13 D. Wang, Z. Xie, M. D. Porosoff and J. G. Chen, *Chem*, 2021, **7**, 2277–2311.
- 14 A. D. N. Kamkeng and M. Wang, *Chem. Eng. J.*, 2023, **462**, 142048.
- 15 Y. F. Zhu, B. Xie, R. Amal, E. C. Lovell and J. Scott, *Small Struct.*, 2023, **4**, 2200285.
- 16 G. Kim, S. Shin, Y. Choi, J. Kim, G. Kim, K.-J. Kim and H. Lee, *JACS Au*, 2022, **2**, 1115–1122.
- 17 R. Tang, Z. Zhu, C. Li, M. Xiao, Z. Wu, D. Zhang, C. Zhang, Y. Xiao, M. Chu, A. Genest, G. Rupprechter, L. Zhang, X. Zhang and L. He, *ACS Mater. Lett.*, 2021, **3**, 1652–1659.
- 18 L. Chen, L. Kovarik and J. Szanyi, *ACS Catal.*, 2021, **11**, 12058–12067.



- 19 D. Zagoraios, S. Tsatsos, S. Kennou, C. G. Vayenas, G. Kyriakou and A. Katsaounis, *ACS Catal.*, 2020, **10**, 14916–14927.
- 20 L. Yang, L. Pastor-Perez, J. J. Villora-Pico, A. Sepulveda-Escribano, F. Tian, M. Zhu, Y.-F. Han and T. R. Reina, *ACS Sustain. Chem. Eng.*, 2021, **9**, 12155–12166.
- 21 Y. Meng, X. Y. Liu, Y. J. Ma, X. H. Gao and X. D. Wen, *Mol. Catal.*, 2022, **529**, 112538.
- 22 A. Pajares, X. Liu, J. R. Busacker, P. Ramirez de la Piscina and N. Homs, *Nanomaterials*, 2022, **12**, 3165.
- 23 J. J. Xu, X. X. Gong, R. R. Hu, Z. W. Liu and Z. T. Liu, *Mol. Catal.*, 2021, **516**, 111954.
- 24 G. Zhou and X. Ai, *Journal of Chongqing Technology and Business University*, 2023, **40**, 8–14.
- 25 Q. Sun, J. Ye, C.-j. Liu and Q. Ge, *Greenhouse Gases*, 2014, **4**, 140–144.
- 26 A. Tsoukalou, P. M. Abdala, D. Stoian, X. Huang, M.-G. Willinger, A. Fedorov and C. R. Mueller, *J. Am. Chem. Soc.*, 2019, **141**, 13497–13505.
- 27 L. Wang, Y. Dong, T. Yan, Z. Hu, A. A. Jelle, D. M. Meira, P. N. Duchesne, J. Y. Y. Loh, C. Qiu, E. E. Storey, Y. Xu, W. Sun, M. Ghousoub, N. P. Kherani, A. S. Helmy and G. A. Ozin, *Nat. Commun.*, 2020, **11**, 2432.
- 28 J. Wang, G. Zhang, J. Zhu, X. Zhang, F. Ding, A. Zhang, X. Guo and C. Song, *ACS Catal.*, 2021, **11**, 1406–1423.
- 29 T. P. Araujo, C. Mondelli, M. Agrachev, T. Zou, P. O. Willi, K. M. Engel, R. N. Grass, W. J. Stark, O. V. Safonova, G. Jeschke, S. Mitchell and J. Perez-Ramirez, *Nat. Commun.*, 2022, **13**, 5610.
- 30 P. C. Zonetti, V. L. Bridi, G. G. Gonzalez, C. R. Moreira, O. C. Alves, R. R. de Avellez and L. G. Appel, *ChemCatChem*, 2019, **11**, 4011–4020.
- 31 M. S. Frei, C. Mondelli, A. Cesarini, F. Krumeich, R. Hauert, J. A. Stewar, D. C. Ferre and J. Perez-Ramirez, *ACS Catal.*, 2020, **10**, 1133–1145.
- 32 X. Zhang, A. V. Kirilin, S. Rozeveld, J. H. Kang, G. Pollefeyt, D. F. Yancey, A. Chojecki, B. Vanchura and M. Blum, *ACS Catal.*, 2022, **12**, 3868–3880.
- 33 T.-y. Chen, C. Cao, T.-b. Chen, X. Ding, H. Huang, L. Shen, X. Cao, M. Zhu, J. Xu, J. Gao and Y.-F. Han, *ACS Catal.*, 2019, **9**, 8785–8797.
- 34 K. Pokrovski, K. T. Jung and A. T. Bell, *Langmuir*, 2001, **17**, 4297–4303.
- 35 H. Zhang, Y. Y. Dong, W. P. Fang and Y. X. Lian, *Chin. J. Catal.*, 2013, **34**, 330–335.
- 36 C. Yang, C. Pei, R. Luo, S. Liu, Y. Wang, Z. Wang, Z.-J. Zhao and J. Gong, *J. Am. Chem. Soc.*, 2020, **142**, 19523–19531.
- 37 C. Y. R. Vera, N. Manavi, Z. Zhou, L.-C. Wang, W. Diao, S. Karakalos, B. Liu, K. J. Stowers, M. Zhou, H. Luo and D. Ding, *Chem. Eng. J.*, 2021, **426**, 131767.
- 38 L. Yao, X. Shen, Y. Pan and Z. Peng, *J. Catal.*, 2019, **372**, 74–85.
- 39 Y. Wei, F. Liu, J. Ma, C. Yang, X. Wang and J. Cao, *Mol. Catal.*, 2022, **525**, 112354.
- 40 N. Siedl, P. Gügel and O. Diwald, *J. Phys. Chem.*, 2013, **117**, 20722–20729.
- 41 C. Gionco, M. C. Paganini, E. Giamello, R. Burgess, C. Di Valentin and G. Pacchioni, *Chem. Mater.*, 2013, **25**, 2243–2253.
- 42 Z. Lu, K. H. Sun, J. Wang, Z. T. Zhang and C. J. Liu, *Catalysts*, 2020, **10**, 1360.
- 43 Y. Cui, L. L. Xu, M. D. Chen, X. B. Lian, C. E. Wu, B. Yang, Z. C. Miao, F. G. Wang and X. Hu, *Catal. Sci. Technol.*, 2019, **9**, 5605–5625.
- 44 K. Stangeland, D. Kalai, H. L. Li and Z. X. Yu, *8th International Conference on Applied Energy (ICAE)*, 2016, vol. 105, pp. 2022–2027.
- 45 G. C. Cabilla, A. L. Bonivardi and M. A. Baltanás, *J. Catal.*, 2001, **201**, 213–220.
- 46 S. S. Dang, B. Qin, Y. Yang, H. Wang, J. Cai, Y. Han, S. G. Li, P. Gao and Y. H. Sun, *Sci. Adv.*, 2020, **6**, eaaz2060.
- 47 L. Z. Gao and C. T. Au, *J. Catal.*, 2000, **189**, 1–15.
- 48 L. Lin, S. Yao, Z. Liu, F. Zhang, N. Li, D. Vovchok, A. Martínez-Arias, R. Castañeda, J. Lin, S. D. Senanayake, D. Su, D. Ma and J. A. Rodriguez, *J. Phys. Chem. C*, 2018, **122**, 12934–12943.
- 49 Y. Wang, L. Zhu, Y. Liu, E. I. Vovk, J. Lang, Z. Zhou, P. Gao, S. Li and Y. Yang, *Appl. Surf. Sci.*, 2023, **631**, 157534.
- 50 S. Kattel, B. Yan, Y. Yang, J. G. Chen and P. Liu, *J. Am. Chem. Soc.*, 2016, **138**, 12440–12450.
- 51 B. Liu, T. Fang and Y. He, *Catal. Sci. Technol.*, 2022, **12**, 300–309.
- 52 W. Wang, Z. Qu, L. Song and Q. Fu, *J. Catal.*, 2020, **382**, 129–140.
- 53 W. Wang, Z. Qu, L. Song and Q. Fu, *J. Energy Chem.*, 2020, **40**, 22–30.
- 54 S. Collins, M. Baltanas and A. Bonivardi, *J. Catal.*, 2004, **226**, 410–421.
- 55 F. Ouyang, J. N. Kondo, K. Maruya and K. Domen, *Catal. Lett.*, 1998, **50**, 179–181.

